J. Fluid Mech. (2007), *vol.* 592, *pp.* 155–175.
doi:10.1017/S0022112007008555 Printed in the United Kingdom

An enthalpy-based hybrid lattice-Boltzmann method for modelling solid–liquid phase transition in the presence of convective transport

SUMAN CHAKRABORTY AND DIPANKAR CHATTERJEE
Department of Mechanical Engineering, Indian Institute of Technology, Kharagpur-721302, India
suman@mech.iitkgp.ernet.in

(Received 27 September 2005 and in revised form 25 July 2007)

An extended lattice Boltzmann model is developed for simulating the convection–diffusion phenomena associated with solid–liquid phase transition processes. Macroscopic hydrodynamic variables are obtained through the solution of an evolution equation of a single-particle density distribution function, whereas, the macroscopic temperature field is obtained by solving auxiliary scalar transport equations. The novelty of the present methodology lies in the formulation of an enthalpy-based approach for phase-change modelling within a lattice-Boltzmann framework, in a thermodynamically consistent manner. Thermofluidic aspects of phase transition are handled by means of a modified enthalpy–porosity formulation, in conjunction with an appropriate enthalpy-updating closure scheme. Lattice-Boltzmann simulations of melting of pure gallium in a rectangular enclosure, Rayleigh–Bénard convection in the presence of directional solidification in a top-cooled cavity, and crystal growth during solidification of an undercooled melt agree well with the numerical and experimental results available in the literature, and provide substantial evidence regarding the upscaled computational economy provided by the present methodology.

1. Introduction

Numerical modelling of solid–liquid phase–transition problems offers a challenge to the research community, primarily attributable to a dynamic evolution of the interfaces and the associated physical, mathematical, as well as computational complexities. As such, issues of resolving multiple physical scales and morphologically complicated deforming domains tax existing computational resources and methods to stringent limits, while executing most of the established strategies of solid–liquid phase-transformation modelling, in practice.

Early efforts in melting/solidification modelling initiated with a moving/deforming grid approach (Rubinsky & Cravahlo 1981; Voller & Cross 1981, 1983; Weaver & Viskanta 1986; Askar 1987), in which the solid–liquid interface must be tracked separately, with additional constraints in the form of interfacial boundary conditions to be imposed on the system of equations. Although this approach worked efficiently for the planar front solidification of pure substances, serious complications arose for solidification problems with more complicated interfacial topologies. Because of these limitations associated with the moving-grid method, the single-domain continuum formulation subsequently emerged as a more attractive proposition, based on the initial pioneering efforts of Bennon & Incropera (1987), which were extended by Voller & Prakash (1987). This method eliminates the need for an explicit tracking of

the solidification fronts, by modelling the entire problem domain with a single set of volume-averaged continuum conservation equations.

Although simulation strategies have become somewhat standardized over the past few decades, serious challenges still exist with regard to the treatment of disparate and physically interconnected length scales characterizing the entire sequence of transport processes. To overcome such difficulties, phase-field models of solidification have been developed and proposed by several workers (Harrowell & Oxtoby 1987; Mikheev & Chernov 1991; Khachaturyan 1996; Beckermann *et al.* 1999; Kim *et al.* 1999; Tong *et al.* 2001). The advantage of the phase-field models is that computational difficulties associated with front tracking are eliminated by introducing an auxiliary-order parameter (the so-called 'phase field') that couples with the evolution of the thermal field. The dynamics of the phase field are designed to follow the evolving solidification front, thereby eliminating the need for any explicit front tracking.

The lattice-Boltzmann (LB) method (Chen *et al.* 1991; Chen, Chen & Matthaeus 1992; Qian, D'Humieres & Lallemand 1992; Succi 2001) has emerged to offer huge potential for solving fluid dynamic problems involving morphological development of complicated phase boundaries (Chen & Doolen 1998; Kendon *et al.* 2001; Sankaranarayanan *et al.* 2002; Barrios *et al.* 2005). The LB method evolved from a Boolean fluid model (Frish, Hasslacher & Pomeau 1986) known as the lattice gas automata (LGA), which simulates fluid motion through particles moving and colliding in a regular lattice. A distinct advantage of this approach, so far as modelling of solid–liquid phase transition problems is concerned, is that the LB method is fundamentally based on microscopic particle models and mesoscopic kinetic equations, which means that micro and meso-scale physics of phase transitions can be elegantly bonded together. Another important advantage, in comparison to the classical continuum based formulation, is that it does not require an immediate explicit calculation of fluid pressure, leading to time-efficient computational simulations. Further, LB models are inherently parallelizable, since the non-localities can be restricted to nearest-neighbour interactions alone, and the only additional computations involved are equivalent to that of a mere streaming step, which renders them suitable to address phase-change processes over large-scale computational domains.

Recognizing some of the above-mentioned natural advantages, De Fabritiis *et al.* (1998) developed a thermal LB model for solving liquid–solid phase transition by employing two types of quasi-particles for liquid and solid phases, respectively. Miller, Succi & Manutti (2001) developed a simple LB model for liquid–solid phase-change processes, using a single type of quasi-particle and a phase-field approach. Further work proceeded along similar lines (Miller & Schroder 2001; Miller 2001; Miller & Succi 2002; Miller, Rasin & Pimental 2004), with the phase-field model acting as a pivotal basis for determining the evolution of respective phase fractions.

Despite possessing a strong fundamental basis, the phase-field model has been found to suffer from certain stringent computational constraints, which originate from the effective phase-field simulation, a mapping between critical characteristics of the phase-field model and the sharp-interface equations, requiring asymptotic expansions in some parameters involving the interface width. Consequently, the phase-field model must use limitingly thin grid spacings, in order to resolve the interfacial region, in principle. Even in the absence of convection, the system of equations that must be solved is strongly nonlinear and coupled in nature, which requires a virtually sharp interface of thickness of the order of few inter-atomic distances to be spread over several grid points. This makes the application of the phase-field

method to solidification problems with small undercooling effects a potentially difficult proposition. For typical microstructures grown at a dimensionless undercooling of 0.1 or less, the ratio of the system size to the minimum grid spacing can be typically greater than 2^{17} or more (Palle & Dantzig 1996), unless adaptive mesh refinement strategies involving computationally involved data structures are used, adding further complications to the overall solution algorithm. This is probably the main reason why phase-field based LB methods, introduced early in the present decade, are not effective in practice, for modelling solid–liquid phase-transition problems.

A fixed-grid enthalpy-based approach may turn out to be a more suitable alternative proposition. In the enthalpy-based methodology, morphological evolution of the phase front can be captured in an implicit manner, through a dynamic update of the pertinent liquid fraction. This update is reflected in the energy conservation equation, as either a heat source or a heat sink. A distinct advantage of this arrangement is that no explicit conditions for energy conservation at the solid/liquid interface need be accounted for (Brent, Voller & Reid 1988). Further, since this approach does not necessitate explicit interface tracking, it is well-suited for treating the continuous transitions between solid and liquid phases, as well as evolution of latent energy over a finite temperature range. Most importantly, the grid-refinement requirements near the interfacial region are not as stringent as in the phase-field method, thereby greatly relaxing the computational constraints. This motivates the development of an alternative LB approach, which potentially retains simplicity, accuracy and parallelizability of the classical LB method and at the same time overcomes most of the practical computational constraints imposed by the phase-field based mathematical modelling approaches.

In this paper, an enthalpy-based hybrid LB technique is proposed for simulating transport phenomena during solid–liquid phase-transition processes, by first developing an appropriate LB method for non-isothermal systems, and a subsequent coupling of the same with a fixed-grid enthalpy–porosity approach (Brent *et al.* 1988). The macroscopic density and velocity fields are simulated using a single particle density distribution function, while the macroscopic temperature field is obtained from coupled scalar transport equations. The newly developed method is subsequently applied to several test cases reported in benchmark studies of solid–liquid phase-change modelling, such as problems involving melting of pure gallium in a rectangular cavity, Rayleigh–Bénard convection during directional solidification of a freezing substance kept in a top-cooled enclosure, and crystal growth during equiaxial solidification of an undercooled melt.

2. Continuum conservation equations

As mentioned earlier, in a classical multiple-domain solidification modelling approach, independent conservation equations for each phase are employed, and are coupled with appropriate boundary conditions at the interfaces. However, such multiple-region solutions require the existence of discrete interfaces between the respective phases, and are generally limited to pure substances. In fact, a major difficulty with regard to their implementation is associated with the tracking of the phase interfaces (which are generally unknown functions of space and time). The need for moving numerical grids and/or coordinate mapping procedures complicates the application of this technique further, and generally, simplifying assumptions regarding the geometric regularity of the interfaces are made. In fact, for topologically complicated interfaces, it would be virtually impossible to track a morphologically

complex zone in a moving/deforming-grid framework. In these situations, a more convenient approach can be a fixed-grid enthalpy-based methodology, in which the transport equations for individual phases are volume-averaged to come up with equivalent single-phase conservation equations, which are valid over the entire domain, irrespective of the constituent phases that are locally present. Further, the interface need not be tracked explicitly, and evolves as a consequence of the solution procedure, by itself. For that purpose, a separate equation for evolution of the liquid fraction is solved, in conjunction with the above set of conservation equations, in order to specify implicitly and update the interfacial locations with respect to space and time. Because of such elegance associated with interfacial modelling in complex solidification problems, a single-domain paradigm (Voller, Swaminathan & Thomas 1990) is employed for the mathematical model discussed in this study.

The equivalent single-phase volume-averaged continuum conservation equations (Brent *et al.* 1988), appropriate for thermo-fluidic transport in the presence of melting/solidification (assuming a Newtonian, laminar and incompressible flow), can be described as follows:

$$\frac{\partial \rho}{\partial t} + \nabla \cdot (\rho \boldsymbol{u}) = 0, \tag{2.1}$$

$$\frac{\partial (\rho \boldsymbol{u})}{\partial t} + \nabla \cdot (\rho \boldsymbol{u}\boldsymbol{u}) = -\nabla p + \nabla \cdot (\mu \nabla \boldsymbol{u}) + \rho \mathbf{G} + \rho \mathbf{S}, \tag{2.2}$$

$$\frac{\partial (\rho C_p T)}{\partial t} + \nabla \cdot (\rho C_p \boldsymbol{u} T) = \nabla \cdot (k_T \nabla T) + \dot{q}, \tag{2.3}$$

where $\rho, \boldsymbol{u}, T$ and p are the density, velocity, temperature and pressure, respectively. In the above equations, μ, C_p and k_T, respectively, are the dynamic viscosity, specific heat and thermal conductivity of the thermodynamic system under consideration. In (2.2), $\boldsymbol{G}$ is an external body force per unit mass, originating out of density gradients prevailing in the domain. For the present model, the above force can be described as: $\boldsymbol{G} = \boldsymbol{g}\beta(T - T_{ref})$, assuming the Boussinesq approximation to be valid, where $\boldsymbol{g}$ is the acceleration due to gravity, β is the volumetric thermal expansion coefficient, and T_{ref} is a reference temperature. The term $\boldsymbol{S}$, appearing in (2.2), represents an equivalent frictional resistance force per unit mass, which originates from the consideration that the morphology of the phase-changing domain can be treated as an equivalent porous medium that offers a frictional resistance towards fluid flow in that region. Mathematically, this can be represented as

$$\boldsymbol{S} = -\boldsymbol{R} \cdot \boldsymbol{u} = -(\mu/\rho)\boldsymbol{K}^{-1} \cdot \boldsymbol{u} \tag{2.4}$$

where $\boldsymbol{R}$ represents an equivalent resistance tensor and $\boldsymbol{K}$ is the permeability tensor. Components of the tensor $\boldsymbol{K}$ depend on the specific morphology of the phase-changing domain, for which any appropriate formulation for flow through a porous medium can be effectively invoked. The primary focus of the present study is not to explore different approaches of porous medium modelling in this regard, but to develop an LB method, based on any chosen porous medium model that is consistent with solid–liquid phase-change morphology. A common approach followed in the literature is to adopt the Darcy model (or some of its variants) for flow through a porous medium, in association with the Cozeny–Kármán equation (Voller & Prakash 1987), as

$$\mu \boldsymbol{K}^{-1} = \kappa \left[\frac{(1 - f_l)^2}{f_l^3 + b} \right], \tag{2.5}$$

where κ is a morphological constant and b is a computational constant introduced to avoid division by zero. Further, f_l is the liquid fraction, given as $f_l = \Delta H/L$, where L is the latent heat of phase change and ΔH is the latent enthalpy of a computational cell undergoing phase change. In (2.5), the term f_l is considered to mimic an equivalent 'porosity' of the cells undergoing phase transition, as for the enthalpy–porosity formulation (Voller & Prakash 1987). This formulation effectively ensures that in phase-changing cells, the porous medium resistance term in (2.2) dominates over the transient, convective and diffusive effects originating out of molecular interaction mechanisms, thereby forcing the velocity field to imitate the Cozeny–Kármán law. On the other hand, in totally solid elements ($f_l = 0$), a large magnitude of the porous medium resistance term forces any velocity predictions effectively to zero. In a fully liquid element ($f_l = 1$), however, this term has no consequence, and the usual form of the Navier–Stokes equation can be retrieved. In essence, it can be summarized that the term, $\boldsymbol{S}$, effectively controls the degree of penetration of the convective field into the interdendritic region.

The latent-heat evolution is accounted for by introducing a source term in the macroscopic energy conservation equation (second term on the right-hand side of (2.3)) as

$$\dot{q} = -\left[\frac{\partial(\rho \Delta H)}{\partial t} + \nabla \cdot (\rho \boldsymbol{u} \Delta H)\right]. \tag{2.6a}$$

For pure material phase change, the term $\nabla \cdot (\rho \boldsymbol{u} \Delta H)$ vanishes and the source term becomes

$$\dot{q} = -\frac{\partial(\rho \Delta H)}{\partial t}. \tag{2.6b}$$

3. Hybrid lattice-Boltzmann method (LBM) for a phase-changing system

The LBM essentially uses the particle velocity distribution function ($f_i(\boldsymbol{x}, t)$) as the primary statistical tool, which quantifies the (real-numbered) probability to observe a pseudo-fluid particle with discrete velocity $\boldsymbol{e}_i$ at lattice node $\boldsymbol{x}$, corresponding to a time, t. The particle-velocity distribution function is defined for particles moving synchronously along the nodes of a discrete regular spatial lattice. The subscripts $i = 0, \ldots, m$ of the velocity vectors indicate their discrete lattice directions on the chosen grid. The fluid particles can collide with each other, as they move under applied forces. In the LBM, the temporal evolution of the particle velocity distribution function, without the influence of any body forces, satisfies a discretized evolution equation of the form:

$$f_i(\boldsymbol{x} + \boldsymbol{e}_i \Delta t, t + \Delta t) - f_i(\boldsymbol{x}, t) = \Delta t \Omega_i, \quad i \in [0, n], \tag{3.1}$$

where Δt is the lattice time step. The left-hand side of (3.1), in effect, represents free propagation of the particle packets along the lattice links. In the presence of a body force, $\boldsymbol{F}_i$ (Martys, Shan & Chen 1998), as an additional external source of momentum, (3.1) is modified to the following form:

$$f_i(\boldsymbol{x} + \boldsymbol{e}_i \Delta t, t + \Delta t) - f_i(\boldsymbol{x}, t) = \Delta t \Omega_i + \Delta t \boldsymbol{F}_i, \quad i \in [1, n]. \tag{3.2}$$

In (3.1) and (3.2), the symbol Ω_i represents a collision operator. In general, the collision term appearing in (3.2) may be linearized, by assuming that there is always a local equilibrium particle distribution, f^{eq}, which depends only on the locally conserved mass and momentum density. A first-order approximation for the collision

operator, accordingly, leads to the following expression:

$$\Omega_i^*(f_i(\boldsymbol{x},t)) = \Omega_i^*\left(f_i^{eq}(\boldsymbol{x},t)\right) + \Omega_i^*\left(f_i(\boldsymbol{x},t) - f_i^{eq}(\boldsymbol{x},t)\right). \tag{3.3}$$

Since Ω_i now only acts on the departure from equilibrium, the first term on the right-hand side of (3.3) vanishes. A convenient formulation for the remainder, used by most current versions of the LB automaton, including the present study, assumes the form of a single-step relaxation, in accordance with the Bhatnagher–Gross–Krook (BGK) approximation (Bhatnagar, Gross & Krook 1954), as follows:

$$\Omega_i = -\frac{1}{\tau}\left(f_i(\boldsymbol{x},t) - f_i^{eq}(\boldsymbol{x},t)\right), \tag{3.4}$$

In (3.4), the relaxation time, τ, is a parameter which quantifies the rate of change towards local equilibrium for incompressible isothermal materials. The BGK relaxation yields maximal local randomization, as particle distributions relax at the same rate, $\omega = 1/\tau$, towards their corresponding equilibrium value. As was first pointed out by Qian *et al.* (1992), the relaxation rate must obey the constraint $0 < \omega < 2$, for the method to be stable and for the particle density and viscosity to be positive. For non-isothermal flows or fluids with variable density, the relaxation time (τ^*) may deviate from a constant according to the following relationship:

$$\tau^* = \tfrac{1}{2} + \frac{1}{\xi(\boldsymbol{x},t,T)}\left(\tau - \tfrac{1}{2}\right), \tag{3.5}$$

where T is the temperature, and $\xi(\boldsymbol{x},t,T)$ is the local particle density (which can be calculated as the local sum over the particle-velocity distribution, according to the relationship)

$$\xi(\boldsymbol{x},t,T) = \sum_{i=0}^{n} f_i(\boldsymbol{x},t,T),$$

resulting in

$$\nu = c_s^2 \Delta t\left(\tau^* - \tfrac{1}{2}\right), \tag{3.6}$$

where ν is the kinematic viscosity, and $\mathrm{c_s} = 1/\sqrt{3}$ is the lattice sound speed.

Regarding the solution for the evolution of the thermal field, it is noted here that in spite of its success in solving various challenging problems involving isothermal fluids, the LBM has not been successful in reliably handling strongly-coupled and complicated thermal problems over a considerable range of the operating parameters, despite there being continuous work in this area (Succi 2001). As a consequence, the success of the thermal LB equation has been limited, in the sense that it is not yet as competitive as the athermal lattice Boltzmann equation, and it cannot perform as well as traditional CFD methods in many aspects. The difficulties encountered in the thermal LBM are primarily associated with numerical instabilities (Zhang & Chen 2003), difficulties in changing the Prandtl-number value from unity (Chatterjee & Chakraborty 2005, 2006, 2007), and limitations in dealing with a restricted temperature range (unless significantly more speeds are added). Although there have been elaborate discussions on the numerical instability in the thermal LB schemes, so far the issue has by no means been resolved. In this context, it can also be noted that a primary defect in the existing energy-conserving thermal LB models is the coupling between the energy and shear modes of the linearized LB evolution operator. Such a spurious coupling essentially violates the rotational symmetry (isotropy), and hence, is macroscopically forbidden. Further, employing a full set of separate distribution functions to simulate

a passive scalar (such as temperature) is too cumbersome, even though this numerical inefficiency can be improved by using a redundant degree of freedom in some LB models.

As an alternative to the classical thermal LB models, hybrid thermal LB methods have been proposed, by virtue of which the flow simulation is accomplished by using the isothermal LBM, while the temperature field is solved by using auxiliary scalar transport equations (Bartoloni *et al.* 1993; Shan 1997; Lallemand & Luo 2003; Zhang & Chen 2003; Mezrhab, Bouzidi & Lallemand 2004). For improved numerical stabilities, multiple-relaxation-time (MRT) models have also been suggested (Lallemand & Luo 2003), as opposed to the simple BGK approximation.

In the present study, a thermodynamically consistent and simplistic LB approach is essentially adopted and combined with a computationally efficient phase-front-capturing methodology. Accordingly, the thermal-field and phase-fraction distributions are obtained from the numerical solution of auxiliary scalar-transport equations, instead of appealing to separate internal energy density distribution functions. However, special considerations are invoked, so as to ensure that the velocity and pressure fields evolve in a thermodynamically consistent manner; a suitable coupling between the athermal and thermal modules of the numerical scheme is established, through the introduction of an appropriate 'interaction' body-force. The key issue here is to ensure an efficient formalism of energy evolution, while maintaining the overall conservation, by giving due considerations to the particle-interaction contribution of the total energy, which is a function of the relative positions between the particles. Although the particle-interaction mechanisms may be neglected for ideal gases, they must be accounted for in non-ideal systems, in a thermodynamically consistent manner. This, in essence, can be implemented by introducing a 'thermodynamic' body force, in the form of

$$\boldsymbol{F}^{int}(\boldsymbol{x}, t) = -\nabla V(\boldsymbol{x}, t), \tag{3.7}$$

where $V(\boldsymbol{x}, t)$ is an interaction potential, defined as follows (Shan & Chen 1993):

$$V(\boldsymbol{x}, \boldsymbol{x}') = G_{\sigma\bar{\sigma}}(\boldsymbol{x}, \boldsymbol{x}')\psi^{\sigma}(\boldsymbol{x})\psi^{\bar{\sigma}}(\boldsymbol{x}'). \tag{3.8a}$$

Here, $G_{\sigma\bar{\sigma}}(\boldsymbol{x}, \boldsymbol{x}')$ is a Green's function, defined as

$$G_{\sigma\bar{\sigma}}(\boldsymbol{x} - \boldsymbol{x}') = \begin{cases} 0, & |\boldsymbol{x} - \boldsymbol{x}'| > \Delta x, \\ \chi_{\sigma\bar{\sigma}} & |\boldsymbol{x} - \boldsymbol{x}'| = \Delta x, \end{cases} \tag{3.8b}$$

where Δx is the lattice constant, and the parameter $\chi_{\sigma\bar{\sigma}}$ controls the strength and sense of the interaction potential between the phases σ and $\bar{\sigma}$. The parameter ψ^{σ} plays an important role in determining the effective number density for the phase, σ, in the system. The potential function, as introduced in (3.8), effectively incorporates long-range attractive or repulsive forces, as a function of number density of the constituents σ and $\bar{\sigma}$. Because in an LBM, particles reside on lattice sites with fixed inter-particle distances, the number density on each site is an implicit indicator of the average distance between particles. The potential, being proportional to the products of local 'effective masses' (ψ^{σ}, $\psi^{\bar{\sigma}}$), essentially dictates the momentum change due to large-range forces between a particle located at the site $\boldsymbol{x}$ and its nearest neighbours. An explicit form of the potential function has been derived in Shan & Chen (1993), as

$$V = \frac{b\Delta x^2}{2D}\chi\psi^2, \tag{3.9}$$

where $\chi = \chi_{11}$, for a single-component fluid, b represents the discrete number of spatial translation vectors constituting the vector basis of the distribution function, and D is the dimensionality. The above formalism, in essence, recovers an equation of state in the following form (Shan & Chen 1993):

$$p = \frac{\Delta x^2}{D}\left[(1-d_0)\rho + \frac{b}{2}\chi\psi^2(\rho)\right], \tag{3.10}$$

where d_0 is a measure of the compressibility of the fluid system under concern. Thermodynamic phase transitions are expected to occur if p does not monotonically increase with ρ, which is possible if χ (which is related to temperature) is sufficiently negative, monotonically increasing and yet, a bounded function of ρ. The function ψ and the parameter d_0 are chosen in accordance with the guidelines outlined in Shan & Chen (1993), and the pertinent details are not repeated here. The function ψ, for instance, can be chosen in the following form:

$$\psi = \rho_0\left[1 - \exp\left(\frac{-\rho}{\rho_0}\right)\right], \tag{3.11}$$

in order to represent long-range inter-particle forces, with a philosophy similar to the basic postulates introduced towards development of many of the non-ideal equations of state (such as, the van der Waals equation).

Based on the solution of the evolution equation for particle-density distribution, the basic hydrodynamic quantities, such as number density and velocity can be obtained through a straight-forward moment summation, as

$$\rho(x,t) = \sum_i f_i(x,t), \tag{3.12a}$$

$$\rho\boldsymbol{u}(\boldsymbol{x},t) = \sum_i \boldsymbol{e}_i f_i(\boldsymbol{x},t) + \frac{\Delta t}{2}\sum_i \boldsymbol{F}_i, \tag{3.12b}$$

where the body force $\boldsymbol{F}$ incorporates a combined contribution from the buoyancy force ($\boldsymbol{G}$), porous medium resistance ($\boldsymbol{S}$) and the interaction force ($\boldsymbol{F}^{int}$).

For discretization of the velocity space (Shan & He 1998), a D2Q9 model is employed, which is characterized with two-dimensional sub-lattices (equivalent to the number of independent speeds) and 9 spatial translation vectors constituting the vector basis of the distribution function. The discrete velocities for the model can be described as follows:

$$\boldsymbol{e}_i = \begin{Bmatrix} \boldsymbol{0}, & i=0, & 4/9 \\ (\cos[(i-1)\pi/2],\ \sin[(i-1)\pi/2])c, & i=1,2,3,4, & 1/9 \\ \sqrt{2}(\cos[(i-5)\pi/2+\pi/4],\ \sin[(i-5)\pi/2+\pi/4])c, & i=5,6,7,8, & 1/36 \end{Bmatrix} = w_i, \tag{3.13}$$

where $c(=\Delta x/\Delta t)$ is the characteristic speed. The physical space $\boldsymbol{x}$ is discretized into a regular lattice such that $\boldsymbol{e}_i\Delta t$ is in conformity with the distance between two neighbouring grid points. In an incompressible flow limit, the density fluctuations are small ($\sim M^2$, M being the Mach number) (He, Luo & Dembo 1997), and accordingly the equilibrium distribution function becomes (Guo, Zheng & Shi 2002)

$$f_i^{eq} = w_i\rho\left[1 + \frac{\boldsymbol{e}_i\cdot\boldsymbol{u}}{c_s^2} + \frac{\boldsymbol{uu}:(\boldsymbol{e}_i\boldsymbol{e}_i - c_s^2\boldsymbol{I})}{2c_s^4}\right]. \tag{3.14}$$

Analogously, the forcing parameter, $\boldsymbol{F}_i$, can be written as

$$\boldsymbol{F}_i = \omega_i \left(1 - \frac{1}{2\tau}\right) \left[\frac{\boldsymbol{e}_i - \boldsymbol{u}}{c_s^2} + \frac{(\boldsymbol{e}_i \cdot \boldsymbol{u})\boldsymbol{e}_i}{c_s^4}\right] \cdot \{\rho(\boldsymbol{G} + \boldsymbol{S}) + \boldsymbol{F}^{int}\}. \tag{3.15}$$

To satisfy the conservation of mass up to second order in the Chapman–Enskog limit, the forcing is executed in two steps, with one half of the forcing being implemented before the collision step and the remaining half thereafter.

It is important to note here that the numerical stability of the LBM mentioned as above depends on several parameters, including the Mach number, the relaxation time, the Courant–Friedrichs–Levy (CFL) number ($CFL = \Delta t|\boldsymbol{e}_i|/\Delta x$) and the strength of the external force field. In general, owing to explicit Euler-forward-time integration, the source strength must obey a stability restriction in the form (Melchionna & Succi 2004):

$$\frac{|\delta f_i|}{f_i} \sim \frac{|\boldsymbol{F}|\Delta x_{min}}{c_s^2} \ll 1, \tag{3.16}$$

where Δx_{min} represents the minimum grid size of the computational mesh.

4. Solution of the temperature field and phase fraction evolution

In the present study, the spatial and temporal evolution of temperature is solved from a supplemental energy transport equation, (2.3), in accordance with a control-volume-based fully implicit finite-difference method (Patankar 1980). The resultant discretized equation takes the following form:

$$a_P T_P = \sum a_{nb} T_{nb} + b + a_P^0 T_P^0 - \frac{\left(\Delta H_P - \Delta H_P^0\right)}{\Delta t} \Delta \forall, \tag{4.1}$$

where $\Delta\forall$ represents the volume of a computational cell (control volume) having a central nodal point P, and the subscript '*nb*' represents the neighbouring grid points. The superscript '0' represents values obtained at the previous time step. The above represents a system of linear algebraic equations of the same size as the number of discrete nodes. This system is numerically solved by employing a line by line tri-diagonal matrix algorithm (TDMA). Moreover, for a physically consistent solution of the above set of equations, it must be ensured that thermodynamically consistent estimates of the nodal latent heat (ΔH_P) are effectively embedded into the solution procedure itself. Although, no explicit governing differential equation is separately available for prescribing the evolution of ΔH in this context, a thermodynamically consistent estimate of the same can be obtained by deriving a separate equation for evolution of the nodal latent enthalpy, so as to implicitly specify and update the interfacial locations with respect to space and time. To achieve this purpose, dynamic evolution/absorption of latent heat is accounted for by a continuous updating of nodal latent enthalpy values of each computational cell, consistent with the prevailing temperature field. In a physical sense, such an updating attempts to neutralize the difference in the nodal temperature predicted from the energy equation and that dictated by the phase-change considerations. This update is reflected in the energy conservation equation, either as a heat source or as a heat sink, leading to a thermodynamically consistent solution of the system of conservation equations. For a hybrid coupling between the D2Q9 model and the finite-volume stencil, the following polynomials are employed to expand the temperature field in the two-dimensional space for the purpose of profile approximation: $\phi_0 = 1$, $\phi_1 = x$, $\phi_2 = y$,

$\phi_3 = (x^2 - y^2)$, $\phi_4 = xy$, $\phi_5 = (x^2 + y^2)$, $\phi_6 = x(x^2 - y^2)$, $\phi_7 = y(x^2 - y^2)$, $\phi_8 = (x^2 - y^2)^2$; so that $T(x, y) = \sum_i a_i \phi_i(x, y)$. In the bulk fluid/solid domain, the coefficients a_i are determined by enforcing $T(x_j, y_j) = \sum_i a_i \phi_i(x_j, y_j)$, such that $(x_j, y_j) = (0, 0)$, $(\pm 1, 0)$, $(0, \pm 1)$ and $(\pm 1, \pm 1)$.

In order to derive a generalized formalism for nodal latent heat updating, it is noted from (4.1) that the ratio of coefficients of sensible enthalpy ($h_P = C_P T_P$) and latent enthalpy (ΔH_P) turns out to be of the order of a_P/a_P^0, where $a_P^0 = \rho C_P \Delta\forall/\Delta t$. Further, on convergence, we must have: $h_P^{n+1} = h_P^n$ and $\Delta H_P^{n+1} = \Delta H_P^n$, which implies

$$h_P^{n+1} + \frac{a_P^0}{a_P} \Delta H_P^{n+1} = h_P^n + \frac{a_P^0}{a_P} \Delta H_P^n. \tag{4.2a}$$

The above, on rearrangement, yields,

$$\Delta H_P^{n+1} = \Delta H_P^n + \frac{a_P}{a_P^0} \left(h_P^n - h_P^{n+1} \right). \tag{4.2b}$$

Since h_P^{n+1} is not known *a priori*, an iterative estimate of the same must be obtained, consistent with the thermodynamics and kinetics of phase change. A physical basis of (4.2*b*) can be appreciated by referring to the numerical simulation of the plane-front solidification of a pure material, for example, in which the temperature of a solidifying computational cell may tend to reduce erroneously from its freezing-point value, out of pure numerical artefacts, as heat is rejected from the control volume. This is due to the inability of the solver to distinguish precisely between sensible and latent heat components. To rectify the situation, the term $h_P^n - h_P^{n+1}$, which appears in the enthalpy updating formula, (4.2*b*), assumes a value of $C_P \left(T_P^n - T_m \right)$, where T_m is the freezing temperature of the substance, so that this departure of sensible enthalpy from its thermodynamically consistent value is dumped into the correction of nodal latent heat, and the temperature reverts back to the freezing temperature (as demanded from physical considerations), until the cell is completely frozen. This consideration effectively suggests a pertinent choice of $h_P^{n+1} = C_P T_m$, for this specific case. In practice, the second term on the right-hand side of (4.2*b*) may be multiplied by a suitable relaxation factor, λ, in order to aid numerical convergence within inner iterations. However, once convergence is achieved, $\Delta H_P^{n+1} = \Delta H_P^n$, and the relaxation factor becomes inconsequential, so far as the converged values of temperature and phase fraction distribution are concerned.

For situations more general than the simple illustrative example mentioned above, the parameter h_P^{n+1} can be constituted, consistent with pertinent microscopic phase-change considerations (Chakraborty & Dutta 2001). In a general solid–liquid phase-transition process, the phase change may take place over a range of temperature (bounded by the solidus and the liquidus temperatures, corresponding to the local composition) instead of occurring at a single temperature. The procedure for enthalpy update, extendable to such general systems and consistent with the present hybrid model, is outlined as follows.

Step 1. Obtain the temperature–concentration coupling from the phase diagram in a functional form.

Step 2. Calculate the liquidus temperature (T_l) and solidus temperature (T_s) corresponding to the local composition, using step 1.

Step 3. Substitute a governing micro-scale relation for concentration in terms of liquid fraction (for example, lever rule, Scheil's equation), in the functional form of step 1.

Step 4. Express the liquid fraction, f_l, as $\Delta H/L$ and T as, h/C_p in the algebraic form obtained from step 1.

Step 5. Obtain an expression for h_P^{n+1}explicitly, using step 4.

Step 6. Constrain the h_P^{n+1} thus evaluated in meaningful limits, i.e. if $h_P^{n+1} > T_l^n$ then $h_P^{n+1} = T_l^n$ and if $h_P^{n+1} < T_s^n$ then $h_P^{n+1} = T_s$.

5. Simulation results

To verify the applicability of the present enthalpy-based LB model for the case of solid–liquid phase transition processes, the modelling of isothermal melting of pure gallium in a rectangular cavity is first undertaken. As a second case study, Rayleigh–Bénard convection in the presence of directional solidification is simulated, and finally, the problem of crystal growth during solidification of an undercooled melt is discussed. The above three problems are specifically chosen here, because are probably the most frequently addressed phase-change problems referred to, in the pertinent literature of melting/solidification modelling.

5.1. *Melting of pure gallium*

Melting of pure gallium in a rectangular cavity is a standard benchmark problem for validation of phase-change modelling strategies, since reliable experiments in this regard (particularly, flow-visualization and temperature measurements) have been well-documented in the literature (Gau & Viskanta 1986). Brent *et al.* (1988) solved this problem numerically with a first-order finite-volume scheme, coupled with an enthalpy–porosity approach, and observed an unicellular flow pattern, consistent with the experimental findings reported in Gau & Viskanta (1986), whereas Dantzig (1989) obtained a multicellular flow pattern, by employing a second-order finite-element enthalpy–porosity model. Miller *et al.* (2001), again, obtained a multicellular flow pattern while simulating the above problem, by employing an LB model in conjunction with the phase-field method. In all the above cases, the nature of the flow field was observed to be extremely sensitive to problem data employed for numerical simulations. Here, numerical experiments are performed with the same set of physical and geometrical parameters, as adopted in Brent *et al.* (1988). The study essentially examines a two-dimensional melting of pure gallium in a rectangular cavity, initially kept at its melting temperature, with the top and bottom walls maintained by insulating. Melting initiates from the left-hand wall with a small thermal disturbance, and continues to propagate towards the right. The characteristic physical parameters are as follows: Prandtl number $(Pr) = 0.0216$, Stefan number $(Ste) = 0.03912$ and Rayleigh number $(Ra) = 6.057 \times 10^5$. Numerical simulations are performed with a (56×40) uniform grid system, keeping the aspect ratio 1.4 in a 9 speed square lattice (D2Q9) over 6×10^5 time steps (corresponding to 1 min of physical time). The results show excellent agreement with Brent *et al.* (1988). For a visual appreciation of flow behaviour during the melting process, figure 1 is plotted, which shows the streamlines and melt-front location at chosen instants of time, corresponding to the experimental observations of Gau & Viskanta (1986). The melting front remains virtually planar at initial times, as the natural convection field begins to develop. Subsequently, the natural convection intensifies enough to have a pronounced influence on overall energy transport in front of the heated wall. Morphology of the melt front is subsequently dictated by the fluid rising at the heated wall travelling across the cavity and impinging on the upper section of the solid front, thereby resulting in this area melting back beyond the mean position of the front. Thereafter, the shape of

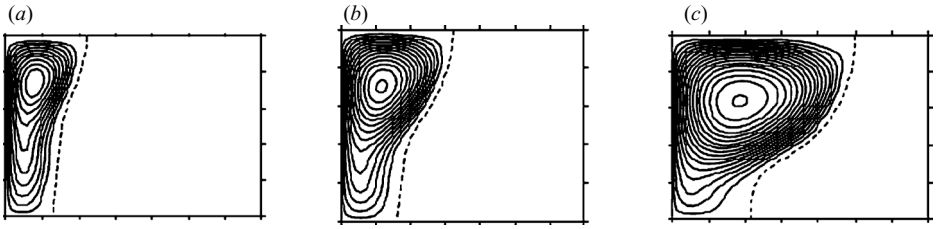

FIGURE 1. Melting of pure gallium in a rectangular cavity (aspect ratio 1.4:1). The cavity is initially filled with solid gallium at a temperature of 28.5 °C. Suddenly, the temperature of the left-hand wall is increased to $T_h = 38\,^{\circ}\mathrm{C}$, with the right-hand wall maintained at the initial temperature. All other boundaries are kept insulated. Important thermophysical properties are characterized by the following dimensionless groups: $Pr = \mu_l C_{p,l}/k_{T,l} = 0.0216$, $Ra = \rho_l^2 C_{P,l} g\beta \Delta T H^3/\mu_l k_{T,l} = 6.057 \times 10^5$, and $Ste = C_{p,l}(T_h - T_m)/L = 0.03912$. The streamlines and melt front locations are shown at (*a*) $t = 6$ min, (*b*) $t = 10$ min, (*c*) $t = 19$ min, from the initiation of melting. The axes limits are as follows: horizontal axis (x/H), 0 to 1.4 and vertical axis (y/H), 0 to 1, where H is the cavity height. The interval between contour lines is 0.05.

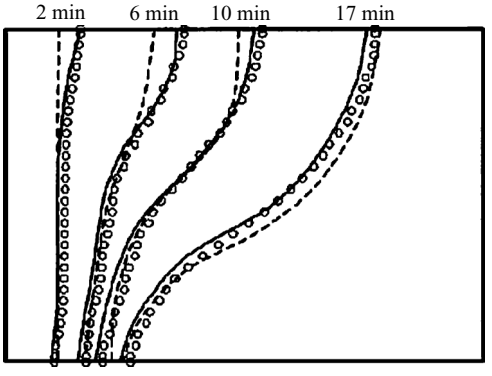

FIGURE 2. Melting of pure gallium in a rectangular cavity (see figure 1 for details): comparison of the interfacial locations, as obtained from the present hybrid LB model (circles), with the corresponding experimental (Gau & Viskanta 1986) results (dotted lines) and continuum-based numerical simulation (Brent *et al.* 1988) predictions (solid line).

the melting front is governed primarily by advection. Overall, agreement can be seen between numerically obtained melt-front positions reported in the benchmark study of Brent *et al.* (1988) and the present simulation. Slight discrepancies between the computed results (both in benchmark numerical work reported earlier and the present computations) and observed experimental findings (Gau & Viskanta 1986) can be attributed to three-dimensional effects prevailing in actual experimental conditions, experimental uncertainties and unaccounted variations in thermo-fluid properties. However, from a comparison of the calculated and experimental (Gau & Viskanta 1986) melt fronts at different times (figure 2), it is found that both the qualitative behaviour and actual morphology of the experimental melt fronts are realistically manifested in the present numerical simulation.

5.2. *Rayleigh–Bénard convection with solidification*

A typical solidifying system in many practical situations is cooling of a melt from the top of a rectangular cavity, in which case there is a strong interaction between unidirectional solidification and Rayleigh–Bénard (RB) convection. Simulations are carried out for solidification of a eutectic ammonium chloride/water (NH_4Cl/H_2O)

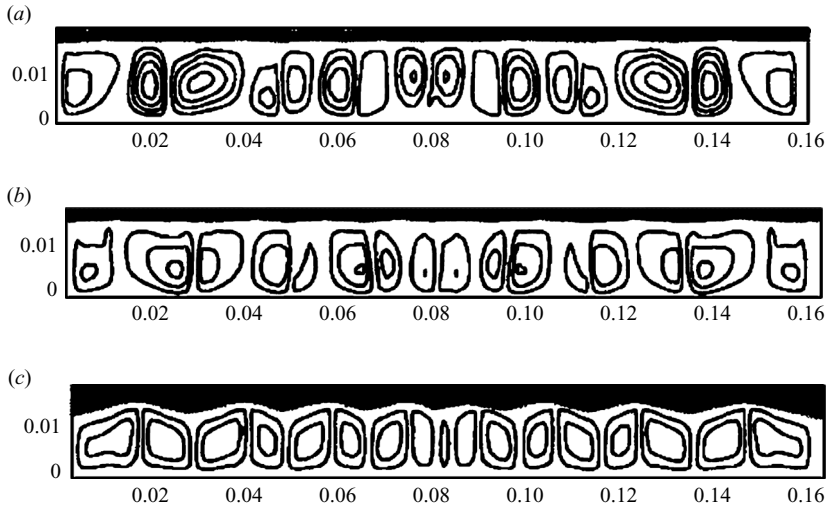

FIGURE 3. Rayleigh–Bénard convection during directional solidification of a eutectic NH_4Cl/H_2O solution in a top-cooled rectangular cavity, with inner dimensions of 160 mm × 17 mm. The horizontal axis represents the dimension of the cavity along the x-direction and the vertical axis represents the same along the y-direction. Different snapshots show the evolution of interface and flow with time, as obtained from numerical simulation at (*a*) $t = 5000$ s, (*b*) $t = 6000$ s, and (*c*) $t = 7500$ s. The interval between contour lines is 0.05. The dark region indicates a solidified zone, and the remaining portion of the domain is in a liquid state. The lines below the solidification interface represent the streamlines of flow. All dimensions are in ms.

solution in a two-dimensional rectangular cavity. Physical and geometrical parameters for this study are taken from Kumar *et al.* (2002). Solidification is initiated by cooling the cavity from the top, while the side faces are kept insulated. Numerical calculations are performed in a square lattice (D2Q9) and the computational domain consists of a uniform 160×20 grid with an aspect ratio of 8. Once liquid in the vicinity of the top wall attains a temperature lower than the freezing point of the mixture, nucleation begins, subsequently leading to the formation of a stable solid front. A cellular flow pattern is observed below the interface, which interacts with the same to give the front a wavy appearance, characterized by multiple crests and troughs. The solidification rate is retarded near zones where warm fluid streams rise towards the interface, leading to the formation of a trough. On the other hand, the rate of solidification is enhanced at locations experiencing downward motion of colder fluid, resulting in the formation of a crest. Subsequently, the cellular convective flow in the presence of an evolving interface tends to weaken, as the solidification front advances (i.e. the effective Rayleigh number decreases). Eventually, the flow dies down as the effective Rayleigh number corresponding to the liquid-layer height falls below a critical value of approximately 1708, analogous to the classical Bénard convection. The results obtained are compared with the experimental work of Kumar *et al.* (2002), and excellent agreement is observed. The evolution of the solidification interface is depicted in figure 3, which shows the numerically obtained interface locations as well as the flow streamlines. The time evolution of the height of the solidified layer is summarized in figure 4. There is excellent agreement between experimental observations (Kumar *et al.* 2002) and computational solutions.

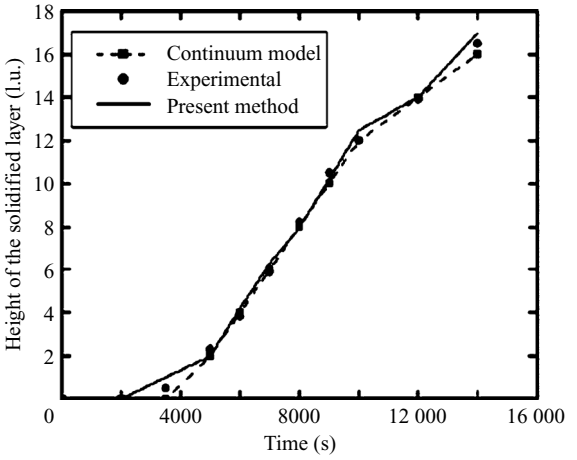

FIGURE 4. Time evolution of the height of the solidified layer, corresponding to the results in figure 3.

5.3. *Crystal growth during solidification*

In this subsection, the problem of crystal growth during solidification of an undercooled melt is discussed. Such a problem is significant because the microstructure of a solidified material, to a large extent, is established during the solidification process. A common microstructure for crystals is often dendritic in nature, and therefore substantial efforts have been directed towards understanding the evolution of this kind of microstructure.

Various numerical methods have been developed to solve the difficult problems associated with dendritic crystallization. Most of the recent efforts in this regard have been based on the phase-field models (Tong *et al.* 2001; Jeong, Goldenfeld & Dantzig 2001; Lan *et al.* 2002), which are characterized by demanding computational constraints, as explained earlier. In the light of the successful application of the LBM to solve such intricate problems, there are two major issues that the methodology must address. First, a topologically complex moving solid–liquid interface must be tracked. Secondly, it must be computationally efficient, since these problems are usually parabolic in nature, with stringent restrictions on the time step and small spatial scales that require sufficient grid resolution.

For numerical implementation of the hybrid LBM for solving problems related to dendritic growth of crystals in an undercooled melt, it must first be recognized that physical processes accompanying a dendritic solidification (such as the diffusional redistribution of chemical species, the generation of interfacial curvature, and the attachment of atoms to the growing solid) require a driving free energy, which can be manifested in terms of an equivalent interfacial undercooling. This implies that there is a consequent deviation of the phase-change temperature from the equilibrium freezing point of the pure material, which is accounted for by the following definition of the function h_P^{n+1}, in the enthalpy updating expression, (4.2*b*):

$$h_P^{n+1} = C_P(T_m - \Gamma^n C^n), \tag{5.1}$$

where T_m is the equilibrium freezing temperature in the presence of a flat interface, and the superscripts n and $n+1$ refer to iteration levels. The Gibbs–Thomson coefficient, Γ, is a function of surface energy (σ) between liquid and solid and the entropy of fusion ($\Delta S_f = L/T_m$). In the presence of solutal transport, such as in the case of binary

systems for example, an additional term $m_l C_l^*$ must be added in the parentheses of (5.1), to take into account the effects of solutal undercooling (where m_l is the local slope of the liquidus line in the phase diagram, and C_l^* is the corresponding liquid phase concentration of the pertinent solute). The curvature, C, at any interface site, is calculated by employing the following expression (Shin & Hong 2002):

$$C = \frac{2\sqrt{\pi}}{l_c}\left[1 - \frac{2}{9}\sum_{m=-1}^{1}\sum_{n=-1}^{1}(1 - f_l)_{m,n}\right], \tag{5.2}$$

where l_c is the inter-grid spacing ($=\Delta x = \Delta y$), and $(m, n) = (0, 0)$ represents the nodal point (P) under consideration, with other values of the indices m and n referring to the neighbouring grid points (nb). In effect, a convex curvature leads to a positive value of C, which subsequently reduces the freezing temperature at that site.

The anisotropy in solid–liquid interfacial energy has a significant effect on dendrite growth. Because of anisotropy, dendrite arms prefer to grow in some specified crystallographic directions depending on the basic lattice structure of the metal. For a cubic metal (body-centred cubic or face-centred cubic), there are four mutually perpendicular preferred growth directions in a two-dimensional situation. In three dimensions, three are six. In the present model, anisotropic effects are inherently accommodated by updating the latent enthalpy content of the interface cells (nearest neighbours) in accordance with the same, thereby imposing constraints over growth conditions perpendicular to the respective faces of computational cells. A precise control over the same is effectively achieved by employing a direction-dependent anisotropy strength, through imposition of the following form of modified Gibbs–Thomson coefficient (Shin & Hong 2002):

$$\Gamma = \Gamma_0(1 - \gamma_t \cos 4\beta), \tag{5.3a}$$

where γ_t represents the thermodynamic anisotropy and β is the angle between local interfacial normal direction and the x-axis, which is obtained as:

$$\beta = \tan^{-1}\left(\frac{-\partial f_l/\partial y}{\partial f_l/\partial x}\right). \tag{5.3b}$$

Here, Γ_0 is the Gibbs–Thomson coefficient in the absence of anisotropic effects ($\Gamma_0 = \sigma_0/\Delta S_f$, where σ_0 is the corresponding interfacial energy).

Another important factor that strongly influences dendritic growth is thermal modulation (noise), which must be taken into account. Such fluctuations can occur at the atomic level, or may originate from system noise. In the present modelling of dendrite growth, thermal fluctuations may be incorporated following a probabilistic growth model instead of a deterministic one, since thermal noises generated are statistically random in nature. The existence of thermal fluctuations mathematically implies here that there exists a finite probability of the fraction of solid becoming 1, even when the fraction of solid according to the macroscopic governing equation is less than 1. This is mathematically modelled as follows (Sasikumar & Sreenivasan 1994; Pal *et al.* 2006): in each iteration, M random numbers (between 0 and 1) are generated for each cell, and each of them is multiplied by L (latent heat of fusion). If the latent enthalpy content (ΔH) of a particular cell is found to be less than the product (random number $\times L$) N times out of M trials, then the ΔH of the cell is changed to zero. When ΔH of a cell becomes zero, its solid fraction automatically changes to one. Thus, the level of thermal fluctuation can be implicitly adjusted by varying the values of N and M. Under any circumstances, the updated latent enthalpy

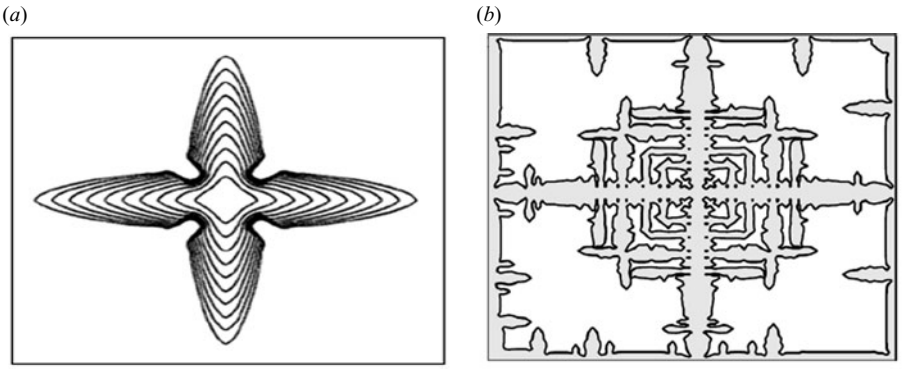

FIGURE 5. Simulated dendritic morphologies in the absence of fluid flow, in a square domain of size $40\,\mu m \times 40\,\mu m$, corresponding to a thermal undercooling of 10 K. Equiaxial dendrites grow in an undercooled melt as a consequence of heat extraction occurring through the liquid. (*a*) Dendritic envelopes at $t/t_{ref} = 10$, where $t_{ref} = l_{ref}^2/\mu_k \Gamma_0$, with $l_{ref} \sim 10^{-5}$ m. The interval between solid fraction contour lines is 0.05, and thermal noise mechanisms are not activated. (*b*) Solidified phase fraction distribution (grey-scale image) at $t/t_{ref} = 1000$, with thermal noise mechanisms activated.

in (4.2*b*) is constrained within physically realistic limits as follows:

$$\begin{aligned} \Delta H &= 0 \quad \text{if} \quad \Delta H < 0, \\ &= L \quad \text{if} \quad \Delta H > L, \end{aligned} \tag{5.4}$$

L being the corresponding latent heat of fusion. Finally, the local liquid fraction can be obtained as

$$f_l = \Delta H / L, \tag{5.5}$$

which distinguishes the presence of liquid and solid phases and their evolution during transients of the solidification process.

For numerical simulations, following physical parameters are considered: $T_m = 933$ K, $\gamma_t = 0.3$, $\Gamma_0 = 2 \times 10^{-7}$ m K, $\sigma_0 = 0.093$ J m^{-2}, $L = 4 \times 10^5$ J kg^{-1}, $\mu = 0.0014$ Pa s, $\rho = 2475$ kg m^{-3}, $C_p = 1000$ J kg^{-1} K^{-1}, $k_T = 200$ W m^{-1} K^{-1}. Overall, a 50×50 uniform grid system is chosen to discretize a square domain of size $40\,\mu m \times 40\,\mu m$. Computations are first carried out to depict the characteristic features of dendritic growth in absence of any fluid flow (figure 5), corresponding to a thermal undercooling of 10 K. As observed from figure 5, the equiaxial dendrites grow in an undercooled melt as a consequence of heat extraction occurring through the liquid. Ahead of dendrite tips, i.e. on the liquid side, there exist negative temperature gradients. The latent heat produced during the dendritic growth flows down the negative gradient in the supercooled melt. This sets up the necessary conditions for an instability, governing the subsequent growth of thermal dendrites (figure 5*a*). As time progresses, the dendrite arms coarsen, because some of the arms, which form initially, become unstable during the progress of solidification and dissolve while others continue to grow. The distinctive curvature undercoolings at different locations cause the larger particles to grow at the expense of the smaller ones. The smaller particles eventually remelt completely, while the mean radius of the remaining particles increases with time. At later times, several closely spaced particles coalesce. Eventually, the side branches from adjacent primary trunks must join, as the fraction of solid increases. The process of side-branch bridging, however, is often delayed until the late stages of solidification. When two adjacent side branches collide with near-perfect

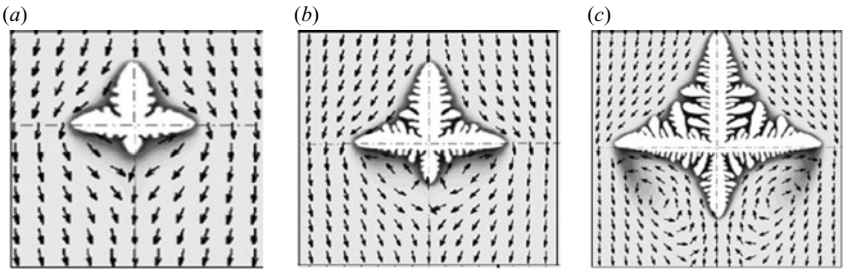

FIGURE 6. Evolution of dendritic morphology under forced flow with a vertically downward free-stream velocity of 0.01 m s^{-1}, while other conditions remain the same as those considered for the pure diffusional crystal growth (figure 5). The three snapshots depict a qualitative picture of the fluid flow and dendritic morphology, corresponding to (*a*) $t/t_{ref} = 10$, (*b*) $t/t_{ref} = 100$, (*c*) $t/t_{ref} = 1000$.

alignment of their parabolic tips, bridging occurs quite rapidly at the tips. When they are misaligned, bridging is delayed and occurs farther behind the primary dendrite tips. To form an equiaxial grain structure, solid particles nucleate, grow and impinge. Although the major structures grow symmetrically, the small side-branch disturbances emanating from the primary arms may grow somewhat asymmetrically, with the extent of asymmetry strongly dependent on the thermal noise. These effects, however, are virtually overweighed by the occurrence of surface-tension-driven coarsening, which become effective when the driving force for growth (supercooling) becomes very small. It happens when an almost isothermal stage is reached in the domain. At this stage, the effect of radius of curvature on freezing point becomes relatively more important. The dendrite arms that have regions of smaller-than-average radius of curvature grow at a slower rate than their neighbours, or melt away because at the isothermal stage, the interface sites with positive curvature have a freezing point slightly below the average temperature and those with negative curvature have a freezing point slightly above the average temperature. This also leads to the so-called competitive growth of dendrite arms (figure 5*b*).

Figure 6 depicts the role of convection on equiaxial dendritic growth in a supercooled melt, under the same thermal conditions as mentioned above. The imposed forced flow velocity at the top boundary is taken to be 0.01 m s^{-1}. In the upstream side (top), convection opposes heat diffusion, which subsequently reduces the thermal boundary-layer thickness and increases local temperature gradients, leading to a faster growth of the upper dendritic arm. Evolution of the downstream arm (bottom), on the other hand, is relatively retarded, for identical reasons. Cool melt is transported from the upstream towards the crystal, causing a steeper temperature gradient in the vicinity. On the downstream side, secondary branches are prevented from growing, since warm fluid is transported around the tip and is pushed along the solid–liquid interface. This flow, in effect, hinders the growth of secondary branches on the downstream main stem. At the tip of the dendrites, there is a compressed boundary layer, which increases the local Péclet number. The compressed isotherms promote the growth of small disturbances that would otherwise be barely consequential. On the upstream side of the main stem, most of the side branches are large. In between some of the large side branches, there are some small side branches. These small side branches have almost stopped growing because they are effectively shielded from the cold melt. As time progresses, side branches are also promoted on the downstream side, which is attributable to the formation of two localized flow vortices of nearly

	Grid requirement		CPU Time (h)	
Method of solution	Gallium melting	Crystal growth	Gallium melting	Crystal growth
Enthalpy-based continuum method (Brent *et al.* 1988)	42×32 Aspect ratio: 1.4	–	26 in an AT & T 3B2/400 microcomputer (19 min melt time)	–
Phase-field-based continuum method (Sasikumar & Jacob 1996)	–	160×320	–	23 per 1 min physical time on a HP-C200 workstation
Phase-field-based LB method (Miller *et al.* 2001)	400×560	200×200	24 per 1 min physical time on a midrange workstation	24 per 1 min physical time on a midrange workstation
Enthalpy-based LB method (present study)	56×40 Aspect ratio: 1.4	50×50 Aspect ratio: 1	2 per 1 min physical time on a PIV 2.8 GHz PC	3 per 1 min physical time on a PIV 2.8 GHz PC

Table 1. Comparison in terms of speed and simulation size.

	Gallium melting		Crystal growth	
Grid size	Maximum relative error (%) in stream function	Maximum relative error (%) in temperature	Maximum relative error (%) in stream function	Maximum relative error (%) in temperature
50×50	–	–	0.94	0.89
100×100	–	–	0.93	0.88
120×120	–	–	0.92	0.87
200×200	–	–	0.92	0.87
56×40	0.86	0.79	–	–
120×86	0.85	0.78	–	–
196×140	0.85	0.77	–	–
252×180	0.85	0.77	–	–

Table 2. Grid sensitivity study.

identical strength. The vortices separated behind the main stem transport cold bulk flow, which meets the downstream side of the main stem and promotes solidification in the vicinity. The individual tips of the side branches do not grow radially, rather, they grow in the direction of the preferred horizontal lattice orientations.

5.4. *A comparative computational assessment of the proposed methodology*

Table 1 a compares the present model with other standard melting/solidification models reported in the literature, in terms of simulation mesh size and the CPU time. The comparison shows that the present enthalpy-based LB method requires considerably less CPU time for effective simulation of generic phase-change problems benchmarked in the contemporary literature, as compared to other existing methodologies. A comprehensive grid-sensitivity study is also carried out, and is presented in table 2. The percentage error with respect to streamfunction and temperature predictions does not change appreciably with mesh refinement, beyond a critical limit, which turns out to be much coarser than the threshold mesh size necessary for implementation of other commonly employed mathematical models,

for identical purposes. This, in turn, demonstrates the effectiveness of the proposed methodology, from the viewpoint of a tradeoff between numerical accuracy and computational economy.

6. Summary

To summarize, the proposed hybrid LB scheme is found to be accurate and attractive for simulating thermofluidic transport during melting/solidification problems. Because of its inherent simplicity in implementation, stability and accuracy, the proposed method might potentially be a powerful tool for solving complex phase-change problems in physics and engineering, characterized by complicated interfacial topologies. Compared with the phase-field-based LB models, the present scheme is implementationally much simpler, since limitingly thin grid spacings are not required to resolve characteristic length scales over the interfacial regions. Although a finer mesh size would result in a better-resolved interface and a more accurate capturing of gradients of field variables, the mesh size for the present model merely plays the role of a synthetic microscope to visualize topographical features of the interface morphology.

REFERENCES

Askar, H. G. 1987 The front tracking scheme for the one-dimensional freezing problem. *Intl J. Numer. Meth. Engng* **24**, 859–869.

Barrios, G., Rechtman, R., Rojas, J. & Tovar, R. 2005 The lattice Boltzmann equation for natural convection in a two-dimensional cavity with a partially heated wall. *J. Fluid Mech.* **522**, 91–100.

Bartoloni, A., Battista, C., Cabasino, S. *et al.* 1993 LBE simulations of Rayleigh–Bénard convection on the APE100 parallel processor. *Intl J. Mod. Phys.* C **4**, 993–1006.

Beckermann, C., Diepers, H.-J., Steinbach, I., Karma, A. & Tong, X. 1999 Modeling melt convection in phase-field simulations of solidification. *J. Comput. Phys.* **154**, 468–496.

Bennon, W. D. & Incropera, F. P. 1987 A continuum model for momentum, heat and species transport in binary solid–liquid phase-change systems. I. Model formulation. *Intl J. Heat Mass Transfer* **30**, 2161–2170.

Bhatnagar, P. L., Gross, E. P. & Krook, M. 1954 A model for collision processes in charged and neutral one-component system. *Phys. Rev.* **94**, 511–525.

Brent, A. D., Voller, V. R. & Reid, K. 1988 Enthalpy-porosity technique for modeling convection–diffusion phase change: application to the melting of a pure metal. *Numer. Heat Transfer* **13**, 297–318.

Chakraborty, S. & Dutta, P. 2001 A generalized formulation for evaluation of latent heat functions in enthalpy-based macroscopic models for convection–diffusion phase change process. *Metall. Mat. Trans.* B **32**, 562–564.

Chatterjee, D. & Chakraborty, S. 2005 An enthalpy based lattice Boltzmann model for diffusion dominated solid–liquid phase transformation. *Phys. Lett.* A **341**, 320–330.

Chatterjee, D. & Chakraborty, S. 2006 A hybrid lattice Boltzmann model for solid–liquid phase transition in presence of fluid flow. *Phys. Lett.* A **351**, 359–367.

Chatterjee, D. & Chakraborty, S. 2007 An enthalpy-source based lattice Boltzmann model for conduction dominated phase change of pure substances. *Int. J. Therm. Sci.* (accepted).

Chen, H., Chen, S. & Matthaeus, W. H. 1992 Recovery of the Navier–Stokes equations through a lattice gas Boltzmann equation method. *Phys. Rev.* A **45**, R5339–5342.

Chen, S. & Doolen, G. D. 1998 Lattice Boltzmann method for fluid flows. *Annu. Rev. Fluid Mech.* **30**, 329–364.

Chen, S., Chen, H., Martnez, D. & Matthaeus, W. 1991 Lattice Boltzmann model for simulation of magnetohydrodynamics. *Phys. Rev. Lett.* **67**, 3776–3779.

Chen, Y., Ohashi, H. & Akiyama, M. 1995 Heat transfer in lattice BGK modeled fluid. *J. Stat. Phys.* **81**, 71–85.

Dantzig, J. A. 1989 Modeling liquid–solid phase changes with melt convection. *Intl J. Numer. Meth. Engng* **28**, 1769–1785.

De Fabritiis, G., Mancini, A., Mansutti, D. & Succi, S. 1998 Mesoscopic models of liquid/solid phase transitions. *Intl J. Mod. Phys.* C **9**, 1405–1415.

Frisch, U., Hasslacher, B. & Pomeau, Y. 1986 Lattice-gas automata for the Navier–Stokes equation. *Phys. Rev. Lett.* **56**, 1505–1508.

Gau, C. & Viskanta, R. 1986 Melting and solidification of a pure metal on a vertical wall. *J. Heat Transfer* **108**, 174–181.

Guo, Z., Zheng, C. & Shi, B. 2002 Discrete lattice effects on the forcing term in the lattice Boltzmann method. *Phys. Rev.* E **65**, 046308-1–046308-6.

Harrowell, P. R. & Oxtoby, D. W. 1987 On the interaction between order and a moving interface: dynamical disordering and anisotropic growth rates. *J. Chem. Phys.* **86**, 2932–2942.

He, X., Luo, L.-S. & Dembo, M. 1997 Some progress in lattice Boltzmann method: enhancement of Reynolds number in simulations. *Physica* A **239**, 276–285.

Jeong, J. H., Goldenfeld, N. & Dantzig, J. A. 2001 Phase field model for three-dimensional dendritic growth with fluid flow. *Phys. Rev.* E **64**, 041602 (1–14).

Kendon, V. M., Cates, M. E., Pagonabarraga, I., Desplat, J.-C. & Bladon, P. 2001 Inertial effects in three-dimensional spinodal decomposition of a symmetric binary fluid mixture: a lattice Boltzmann study. *J. Fluid Mech.* **440**, 147–203.

Khachaturyan, A. G. 1996 Long-range order parameter in field model of solidification. *Phil. Mag.* A **74**, 3–14.

Kim, Y-T., Provatas, N., Goldenfeld, N. & Dantzig, J. A. 1999 Universal dynamics of phase-field models for dendritic growth. *Phys. Rev.* E **59**, R2546–R2549.

Kumar, P., Chakraborty, S., Srinivasan, K. & Dutta, P. 2002 Rayleigh–Bénard convection during solidification of a eutectic solution cooled from the top. *Metall. Trans.* B **33**, 605–612.

Lallemand, P. & Luo, L.-S. 2003 Hybrid finite-difference thermal Lattice Boltzmann equation. *Intl J. Mod. Phys.* B **17**, 41–47.

Lan, C. W., Hsu, C. M., Liu, C. C. & Chang, Y. C. 2002 Adaptive phase field simulation of dendritic growth in a forced flow at various supercoolings. *Phys. Rev.* E **65**, 061601(1–11).

Martys, N. S., Shan, X. & Chen, H. 1998 Evaluation of the external force term in the discrete Boltzmann equation. *Phys. Rev.* E **58**, 6855–6857.

Melchionna, S. & Succi, S. 2004 Electrorheology in nanopores via lattice Boltzmann simulation. *J. Chem. Phys.* **120**, 4492–4497.

Mezrhab, A., Bouzidi, M. & Lallemand, P. 2004 Hybrid lattice-Boltzmann finite-difference simulation of convective flows. *Computers Fluids* **33**, 623–641.

Mikheev, L. V. & Chernov, A. A. 1991 Mobility of a diffuse simple crystal melt interface. *J. Cryst. Growth.* **112**, 591–596.

Miller, W. 2001 The lattice Boltzmann method: a new tool for numerical simulation of the interaction of growth kinetics and melt flow. *J. Cryst. Growth* **230**, 263–269.

Miller, W. & Schroder, W. 2001 Numerical modeling at the IKZ: an overview and outlook. *J. Cryst. Growth* **230**, 1–9.

Miller, W. & Succi, S. 2002 A Lattice Boltzmann model for anisotropic crystal growth from melt. *J. Stat. Phys.* **107**, 173–186.

Miller, W., Succi, S. & Manutti, D. 2001 Lattice Boltzmann model for anisotropic liquid–solid phase transition. *Phys. Rev. Lett.* **86**, 3578–3581.

Miller, W., Rasin, I. & Pimentel, F. 2004 Growth kinetics and melt convection. *J. Cryst. Growth* **266**, 283–288.

Pal, D., Bhattacharya, J., Dutta, P. & Chakraborty, S. 2006 An enthalpy model for simulation of dendritic growth. *Numer. Heat Transfer* B **50**, 59–78.

Palle, N. & Dantzig, J. A. 1996 An adaptive mesh refinement scheme for solidification problems. *Mettal. Trans.* **27A**, 707–717.

Patankar, S. V. 1980 *Numerical Heat Transfer and Fluid Flow*. Hemisphere/McGraw-Hill.

Qian, Y., D'Humieres, D. & Lallemand, P. 1992 Lattice BGK models for Navier–Stokes equation. *Europhys. Lett.* **17**, 479–484.

Rubinsky, B. & Cravahlo, E. G. 1981 A finite element method for the solution of one-dimensional phase change problems. *Intl J. Heat Mass Transfer* **24**, 1987–1989.

Sankaranarayanan, K., Shan, X., Kevrekidis, I. G. & Sundaresan, S. 2002 Analysis of drag and virtual mass forces in bubbly suspensions using an implicit formulation of the lattice Boltzmann method. *J. Fluid Mech.* **452**, 61–96.

Sasikumar, R. & Sreenivasan, R. 1994 Two-dimensional simulation of dendrite morphology. *Acta Metall. Mater.* **42**, 2381–2386.

Shan, X. 1997 Simulation of Rayleigh–Bénard convection using a Lattice Boltzmann model. *Phys. Rev.* E **55**, 2780–2788.

Shan, X. & Chen, H. 1993 Lattice Boltzmann model for simulating flows with multiple phase and components. *Phys. Rev.* E **47**, 1815–1819.

Shan, X. & He, X. 1998 Discretization of the velocity space in the solution of the Boltzmann equation. *Phys. Rev. Lett.* **80**, 65–68.

Shin, Y. H. & Hong, C. P. 2002 Modeling of dendritic growth with convection using a modified cellular automaton model with a diffuse interface. *ISIJ Intl* **42**, 359–367.

Succi, S. 2001 *The Lattice Boltzmann Equation for Fluid Dynamics and Beyond*. Oxford University Press.

Tong, X., Beckermann, C., Karma, A. & Li, Q. 2001 Phase-field simulations of dendritic crystal growth in a forced flow. *Phys. Rev.* E **63**, 061601-(1-16).

Voller, V. & Cross, M. 1981 Accurate solutions of moving boundary problems using the enthalpy method. *Intl J. Heat Mass Transfer* **24**, 545–556.

Voller, V. & Cross, M. 1983 An explicit numerical method to track a moving phase change front. *Intl J. Heat Mass Transfer* **26**, 147–150.

Voller, V. R. & Prakash, C. 1987 A fixed grid numerical modeling methodology for convection–diffusion mushy region phase change problems. *Intl J. Heat Mass Transfer* **30**, 1709–1719.

Voller, V., Swaminathan, C. R. & Thomas, B. G. 1990 Fixed grid techniques for phase change problems: a review. *Intl J. Numer. Methods Engng* **30**, 875–898.

Weaver, J. A. & Viskanta, R. 1986 Freezing of liquid saturated porous media. *Intl J. Heat Mass Transfer* **33**, 2721–2734.

Zhang, R. & Chen, H. 2003 Lattice Boltzmann method for simulations of liquid–vapor thermal flows. *Phys. Rev.* E **67**, 066711(1-6).